This is a repository copy of *CuInS2/ZnS-based QLED design and modelling for automotive lighting systems*.

White Rose Research Online URL for this paper:
https://eprints.whiterose.ac.uk/168554/

Version: Accepted Version

Article:

Santaella, JJ, Critchley, K orcid.org/0000-0002-0112-8626, Rodriguez-Bolivar, S et al. (1 more author) (2020) CuInS2/ZnS-based QLED design and modelling for automotive lighting systems. Nanotechnology. ISSN 0957-4484

https://doi.org/10.1088/1361-6528/abcced

© 2020 IOP Publishing Ltd. This is the Accepted Manuscript version of an article accepted for publication in Nanotechnology. IOP Publishing Ltd is not responsible for any errors or omissions in this version of the manuscript or any version derived from it. The Version of Record is available online at doi.org/10.1088/1361-6528/abcced

Reuse
This article is distributed under the terms of the Creative Commons Attribution-NonCommercial-NoDerivs (CC BY-NC-ND) licence. This licence only allows you to download this work and share it with others as long as you credit the authors, but you can't change the article in any way or use it commercially. More information and the full terms of the licence here: https://creativecommons.org/licenses/

Takedown
If you consider content in White Rose Research Online to be in breach of UK law, please notify us by emailing eprints@whiterose.ac.uk including the URL of the record and the reason for the withdrawal request.

eprints@whiterose.ac.uk
https://eprints.whiterose.ac.uk/

Design and Fabrication of $CuInS_2$/ZnS-based QLED for Automotive Lighting Systems

J.J. Santaella,[†,‡] K. Critchley,[¶] S. Rodríguez-Bolívar,[†,§] and F. M. Gómez-Campos*,[†,§]

†*Departamento de Electrónica y Tecnología de los Computadores, Facultad de Ciencias, Universidad de Granada, 18071, Granada, Spain*

‡*VALEO Lighting Systems, Department of Electronics, Martos, Spain*

¶*School of Physics and Astronomy, University of Leeds, Leeds LS2 9JT, United Kingdom*

§*CITIC-UGR, C/ Periodista Rafael Gómez Montero, 2, Granada, Spain*

E-mail: fmgomez@ugr.es

Abstract

This work reports the design, manufacturing and numerical simulation approach of a 6-pixel (4.5mm^2/pixel) electroluminescent quantum dot light emitting device (QLED) based on $CuInS_2$/ZnS quantum dots as an active layer. The QLED device was fabricated using a conventional multi-layer thin film deposition. In addition, the electrical I-V curves were measured for each pixel independently, observing how the fabrication process and layer thickness have an influence in the shape of the plot. This experimental device, enabled us to create a computational model for the QLED based on the Transfer Hamiltonian approach to calculate the current density J(mA/cm^2), the band diagram of the system, and the accumulated charge distribution. Besides, it is worth highlighting that the simulator allows the possibility to study the influence of different parameters of the QLED structure like the junction capacitance between the distinct multilayer set. Specifically, we found that the Anode-HIL interface capacitance has a greater influence in the I-V curve. This junction capacitance plays an important role in the current density increase and the QLED turn-on value when a forward voltage is applied to the device. The simulation enabled that influence could be controlled by the selection of the optimal thickness and transport layers during the experimental fabrication process. This work is remarkable since it achieves to fit simulation and experiment results in an accurate way for electroluminescent QLED devices; particularly the simulation of the device current, which is critical when designing the automotive electronics to control these new nanotechnology lighting devices in the future.

1 Introduction

Lighting in the automotive world has undergone a radical change in recent years thanks to light emitting device (LED).[1,2] For example, the use of halogen lamps is being replaced by these LEDs. One of the main advantages, apart from the low energy consumption and the long useful life, is the style that these devices offer. The current and future trend in the automotive world is to achieve even greater lighting surfaces with flexible features and shapes in three dimensions (3D) as shown in Fig. 1. However, the current LED technology formed by discrete devices of point light sources makes this task very complex and expensive. Hence, the possibility to find new lighting alternatives for the automotive industry and develop methods to easily simulate the electrical behaviour of these new devices, shape the motivation of this work.

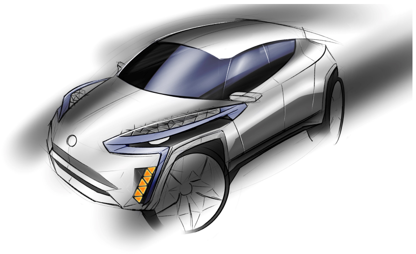

Figure 1: . Automotive lighting system design integration. Headlamps with large and curved light blue surface for DRL (daytime running light).

A nanomaterial called quantum dots (QDs) can end these issues in the automotive field. QDs are nanocrystal semiconductors where electrons are confined in a region of space of nanometric dimensions. Specifically, LED lighting devices based on QDs (quantum dot LEDs), known by their acronym QLEDs (for electroluminescence physical phenomenon), offer a promising future as a new generation of lighting devices due mainly to three factors: purity of color, processibility and stability.[3]

1.1 Cd-free nanoparticles

Cadmium chalcogenide based materials were first nanocrystals studied due to the emission wavelength found in the visible spectrum with high quality optical properties.[4] However, the use of toxic heavy metals such as Cd and Pb is restricted in some countries and the technology trend should avoid them.[4] Therefore, demonstration of high-performing Cd-free QLEDs will likely be crucial to securing widespread industry, particularly automotive field, and government support for those lighting devices.

Nowadays, the main challenge of Cd-free QDs is to achieve at least a performance comparable to Cd-based QDs. Thus, many research groups are looking for new nanochemistry methods to design and fabricate Cd-free quantum dots.[5]

1.2 QDs for Lighting Systems

Over last few years a diversity of Cd-free QDs have been synthesized from materials including indium phosphide (InP),[4,6,7] copper indium sulfide ($CuInS_2$),[8–15] silver indium sulfide ($AgInS_2$),[16–20] ZAISe (Zn-Ag-In-Se),[21] doped Zn chalcogenides,[22,23] graphene,[24] silicon,[25] indium arsenide (InAs),[26–29] Zinc selenide (ZnSe)[30] and Gallium arsenide (GaAs).[31]

Therefore analyzing the materials before, which offer the possibility to be used as the active layer of the QLED, and focusing on emission wavelength and quantum yield (QY) as main parameters to determine the efficiency of the QDs used, it is possible to imagine the best scenario relating to the material selection for lighting systems.

Once a thorough study on the Cd-free materials for the active layer of the QLED has been carried out, it is possible to conclude that indium phosphide (InP) and copper indium sulfide ($CuInS_2$), together with their alloys in the different core/shell structures, are the best candidates to form the active layer of the QLED as shown in Fig. 2

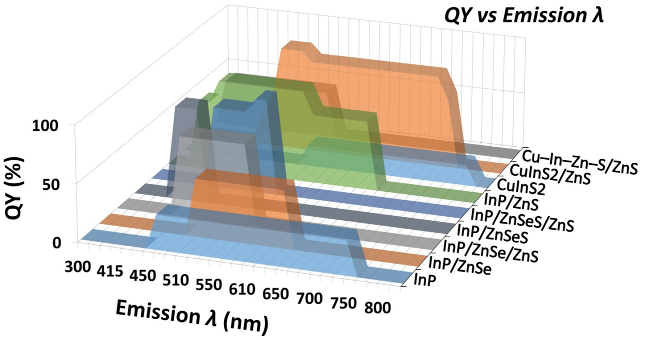

Figure 2: . Emission spectra range vs QY of Cd-free QDs (InP and $CuInS_2$).

The literature shows that more effort has gone into InP as base material for the emitting layer than of $CuInS_2$. When comparing figures of merit between both materials it can be concluded that one of the reason is the large FWHM (full width at half maximum) values that $CuInS_2$ QLEDs ($\sim$100nm) exhibit, probably because of the radiative transitions in donor-acceptor levels and/or the emission from surface defects sites.[26] In fact, it can be twice than InP($\sim$50nm) counterpart which experimentally implies that InP shows a purer color than $CuInS_2$-based QLEDs, which is important for display technology.

Nevertheless, it is easier to achieve deeper red color with $CuInS_2$ QDs which can result in advantages to the design of state-of-the-art automotive lighting systems, particularly taillight applications[32,33] Moreover, the purity of the color in this automotive field relating to FWHM values might not be so critical comparing to electronic consumer displays and therefore great attention should be drawn in $CuInS_2$ QDs as emitting layer to form the QLED. Thus we selected $CuInS_2$/ZnS as the main candidate for the QLED device manufacturing and modelling.

2 $CuInS_2$-based quantum dots

Likewise, environmentally friendly $CuInS_2$-based quantum dots, particularly colloidal $CuInS_2/ZnS$ (core/shell structure) in toluene solvent were acquired commercially from NNCrystal and Mesolight suppliers. Thereby, QD size, absorption & emission spectrum, FWHM and PL QY (photoluminiscence quantum yield) were measured to confirm what was expected from both bibliography and QD supplier datasheet.

2.1 QDs size

High Resolution Transmission Electron Microscopy (HRTEM) Titan® was used to measure the QD size. Thus, Fig. 3 shows the nanoparticles measurement in HRTEM mode, presenting also the histogram extracted.

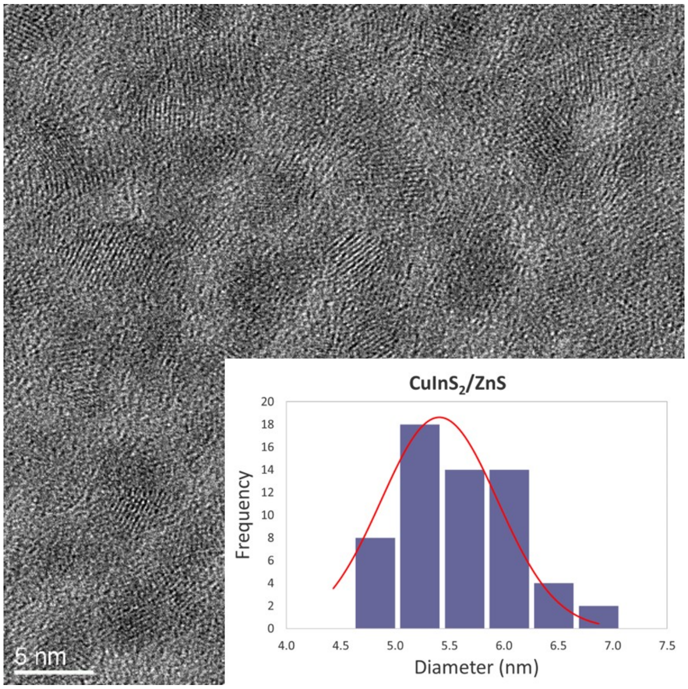

Figure 3: . TEM pictures from (S/TEM) Titan® in transmission mode to calculate the diameter of the QDs core/shell. QDs histogram + normal fit added.

Table 1 shows the diameter results in comparison with datasheet numbers.

Table 1: QDs size (diameter) measurements vs supplier datasheet.

$CuInS_2/ZnS$ QDs	Datasheet(nm)	Measured(nm)
core	3.3±0.5	3.4±0.3
core/shell	5.5±0.5	5.4±0.5

2.2 Absorption, Emission, FWHM and PL QY

UV·VIS·NIR (ultra-violet·visible·near infra-red radiation) spectrophotometer and PL QY spectrometer were used to measure absorption & emission spectrum, FWHM and PL QY. Fig. 4 shows the comparison results with supplier datasheet.

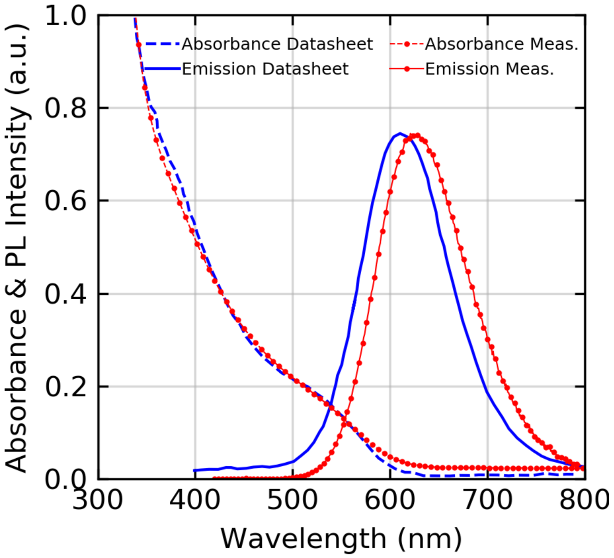

Figure 4: . $CuInS_2/ZnS$ Absorption & Emission spectrum (datasheet vs measured).

Likewise, Table 2 shows the diameter results.

Table 2: QDs parameter measurements vs supplier datasheet.

$CuInS_2/ZnS$ QDs	Datasheet	Measured
PL peak(nm)	611	622
FWHM(nm)	107	108
QY (%)	43	41

These data from the supplier, i.e. size, absorption & emission spectrum, FWHM and QY, were confirmed by the experimental measurements, with minimal deviations between them.

3 QLED Device

Once $CuInS_2$/ZnS QDs were characterized, QLED device was designed, manufactured and electrically characterized. Relating to the QLED structure it comes essential the good selection of the materials to conform the different internal layers. The objective is to obtain the best heterojunction band diagram to make possible the highest recombination rate at the core of the QD active layer and the balance charge injected from cathode and anode.[34] Therefore, the selection of electron and holes injection and transport layer materials along with the blocking electron or hole films are vital to the performance of the whole system.

3.1 QLED Design

Experimental QLEDs based on $CuInS_2$ quantum dots have been reported in the literature. By adapting these reported methods, we constructed a device following the structure[35,36] depicted in Fig. 5. In addition, the bulk material energy levels diagram are shown in the Fig. 6.

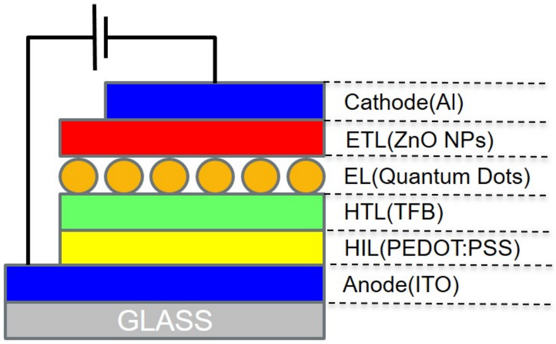

Figure 5: . QLED architecture based on material layers selection.

Once the theoretical structure was designed and the material layers were selected due to the optimal compatibility with the energy levels set as target to achieve, the physical design took place.

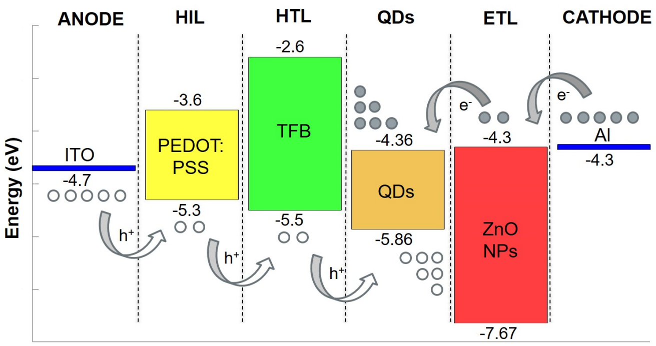

Figure 6: . QLED bulk material energy levels diagram proposed for the different layers in device with respect to vacuum.

3.2 QLED Manufacturing

Likewise, this experimental process was performed following thin-film layer deposition techniques. The QLED manufacturing process followed could be found in many references.[35–37] Those steps were adapted to the one described from Ossila supplier.[38]

3.2.1 Chemicals.

IPA(Isopropyl alcohol), Decon90™, PEDOT:PSS (Poly(3,4-ethylenedioxythiophene) polystyrene sulfonate), TFB(Poly(9,9-dioctylfluorene-alt-N-(4-sec-butylphenyl)-diphenylamine)) (99%), Chlorobenzene (99.8%), $CuInS_2/ZnS$ quantum dots, ZnO NPs (Avantama N-10), Aluminum, UV curable epoxy.

3.2.2 Substrate cleaning.

Substrates were purchased from Ossila with pre-patterned ITO (Indium Tin Oxide) electrodes. It meant that ITO was used for the anode electrode of the QLED. Pre-cleaning routine, to remove dirt and dust, was put in place by using Decon90™ cleaning solution, followed by a sonication bath and UV Ozone clean for 10 minutes creating a pristine and hydrophilic ITO surface.[38]

3.2.3 Layer deposition.

PEDOT:PSS, used for HIL layer, was first filtered using solvent safe syringe ended in a 0.45μm PES (hydrophilic) filter and deposited on the pre-patterned ITO substrate by spin coating technique at 5000 rpm for 30 seconds to produce a film thickness of $\sim$20nm. After cleaning the cathode area with chlorobenzene solvent, the substrate was placed on a hotplate at 150°C for 30 minutes to cure and remove the water from the HIL layer, and placed to cool at ambient temperature.

TFB, used for HTL layer, was preprocessed by making a mix of 8mg/ml concentration in chlorobenzene. The mix was filtered through a solvent safe syringe ended in a 0.1μm PTFE(hydrophobic) filter and deposited just above HIL layer, by spin coating at 4000 rpm for 30 seconds to produce a film thickness of $\sim$30nm. Again, after cleaning the cathode area, the substrate was put on a hotplate at 150°C for 30 minutes to cure, and placed to cool at ambient temperature.

QDs characterized in the previous steps were used as EL layer following same strategy. Then, colloidal quantum dot solutions were deposited on the substrate, just above HTL layer, by spin coating at 2000 rpm for 20 seconds to produce a film thickness of $\sim$20nm. Moreover, after cathode cleaning, the substrate was put on a hotplate at 60°C for 15 minutes to cure, and placed to cool at ambient temperature.

ZnO nanoparticles suspended in 2-propanol were used as ETL layer. They were filtered through a safe syringe ended in a 0.1μm PTFE(hydrophobic) filter and deposited on the substrate, just above EL layer, by spin coating at 1500 rpm for 60 seconds to produce a film thickness of $\sim$35nm. Finally, after ETL deposition, cathode was cleaned and substrate was put on a hotplate at 60°C for 30 minutes to cure, and placed to cool at ambient temperature.

Aluminum, used as cathode, was deposited by thermal evaporation technique to create the last metallic contact. Then, a cathode mask was put inside the vacuum thermal evaporator and $\sim$100nm of Al were deposited on ETL layer with an evaporation rate of 1.5Å/s. Finally, the substrate was placed on a hotplate at 150°C for 15 minutes for annealing purposes, and placed to cool at ambient temperature.

3.2.4 Encapsulation.

After cathode deposition was implemented, an encapsulation process was performed with the goal to protect the devices against degradation by oxygen and moisture. Thus, UV curable epoxy was placed just above the active layer and a glass coverslip on top of the substrate. After that, a curing process was carried out by using a low power UV light (of 380 nm) for 30 minutes.

3.2.5 External metallic contacts.

To complete the manufacturing of the QLED device, metallic legs acquired from Ossila were used to connect and access electrically to each independent pixels anodes and the common cathode electrode. Final QLED device electrically driven is shown in the inset of Fig. 7

3.3 QLED Characterization

Once the QLED was manufactured, the next step was to electrically characterize the lighting device. This experimental design was performed following basic electronics techniques, by using a SMU (Source Meter Unit) to finally obtain the I-V performance curve of each pixel individually and depicted in Fig. 7.

Fig. 7 shows different I-V curves depending on the pixel measured. The current difference shown is due to variability in the manufacturing process. Since it is a prototype where the main thin film deposition technique is performed by spin-coating as laboratory tool, the thicknesses of the different layers that makeup the QLED are not uniform. This leads to different electrical behaviors for each pixel.

According to our model, different electrical behavior found for each individual pixel is explained by the contribution of the capacitance physically attached to each QLED layer. Thereby these capacitive couplings have an important contribution to the total device current. Our model shows how the capacitance at the Anode-HIL interface has a great contribution in the I-V performance.

Furthermore, the localization and structure of the $CuInS_2/ZnS$ QDs in the device prevents lateral charge spreading and Coulomb repulsion of charges into the QDs,[39] being the carrier tunneling, the prominent mechanism for current flowing through the QLED device.

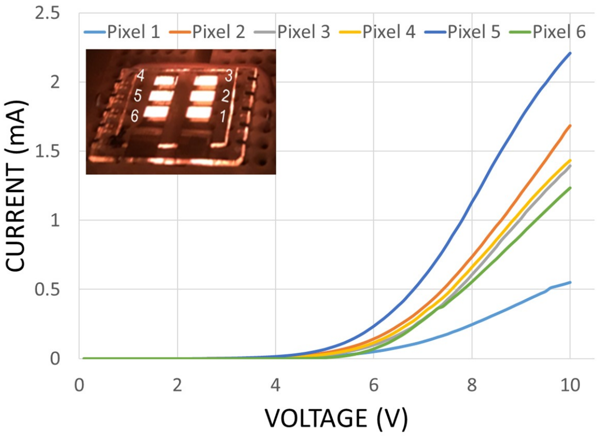

Figure 7: . Figure illustrating the fundamental QLED I-V curve measured and tempted to modelling and simulate.

4 Electrical Modelling

The goal to be achieved consists in creating an electronic transport model for the whole QLED system i.e. anode-ETL-QD-HTL-cathode by simulating the I-V characteristic, the charge distribution and the band diagram of the QLED device to correlate the electrical behavior from QLED designed and manufactured. Likewise, Transfer Hamiltonian approach, developed for interacting Si quantum dots embedded in a SiO_2 dielectric matrix in contact with two electrodes by Illera *et al.*,[40–45] was adapted to the QLED device case.

4.1 Transfer Hamiltonian approach

The Transfer Hamiltonian method was first introduced by Bardeen[46] to the case of solid junctions,[47] to calculate the current passing through a planar tunnel junction when a small bias V is applied between the electrodes.[48]

Furthermore, using that approach the whole system can be described as independent subsystems connected by a transmission probability through the dielectric media.[42] Generally, for a more complex system, it is possible to define the current flowing between two parts (*i,j*) of the latter. Assuming no inelastic scattering and symmetry in the transmission coefficient,[40] the net current flux between two parts of the system can be written as

$$I_{ij} = \frac{4\pi q}{\hbar} \int T_{ij}(E)\rho_i(E)\rho_j(E)(f_j(E) - f_i(E))dE \tag{1}$$

where $T_{ij}(E)$ is the transmission probability, $\rho_i(E)$, $\rho_j(E)$ are the density of states and $f_i(E)$, $f_j(E)$ are the non-equilibrium energy distribution functions in each side of the barrier. Yet, the distribution functions of each part of the system are unknown.[42]

4.2 The QLED model

After analyzing the previous work from Illera *et al.*, our particular device has a different application (lighting system) and therefore a distinct working physics architecture. As generally explained below, it implies a different adaptation of the Transfer Hamiltonian method to the QLED device experimentally fabricated in this work. Therefore, the main differences are raised from quantum dots used i.e. Si/ SiO_2 (Illera *et al.* work) and $CuInS_2$/ZnS (present work), and new transport layers introduced as shown in Fig. 5 and Fig. 6.

Moreover, to adapt the particular QLED system developed in this work to the theoretical approach made by Illera *et al.*, the Transfer Hamiltonian approach has been followed taking into account all layers and not only the quantum dots. Thus, transport layers and QD layers have been processed as individual subsystems associating a Non Coherent Rate Equation (NCRE) for each one. Furthermore, the interactions between all layers are introduced by transition rates and capacitive couplings taking into account the density of states (DOS) of each subsystem. Finally, to solve the multielectron problem, the effects of the local potential are computed within the self-consistent field (SCF) regime in the same way proposed by Illera *et al.* Likewise, the QLED system modelled in this work is depicted in the Fig. 8.

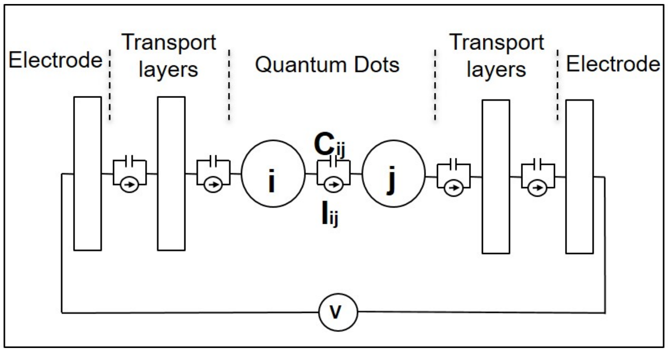

Figure 8: . QLED model proposed with all transport layer form experimental device introduced i.e. Anode/HIL/HTL/QDs/ETL/Cathode.

4.2.1 Total charge.

As well described by Illera *et al.* and in equilibrium state, the electrochemical potential is the same throughout the whole system, being the current between any two parts of the system equal to zero.

$$I_{ij} = 0 \tag{2}$$

Now, if an external bias voltage (V) is applied at the electrodes, the whole system is driven out of equilibrium,[40] creating carrier currents as a consequence of the different population in each electrode.[41] Thereby, the electrochemical potential of the electrodes became as follows

$$\mu_L - \mu_R = qV \tag{3}$$

Likewise, the total charge inside each QLED layer (i) takes the usual definition,

$$N_i = \int \rho_i\,(E) n_i(E) dE \tag{4}$$

Where both $\rho_i(E)$ and $n_i(E)$ are the density of states (DOS) and the energy distribution functions (unknown) for each layer (i) respectively.[42] For the sake of clarity and following Illera *et al.* work, the energy distribution function for each layer (i) from the QLED will be defined as *n_i(E)*, while *f_L(E)* and *f_R(E)* will be reserved for the energy distribution function of the left and right electrodes. Then, it is possible to write the evolution of the charge over time as follows[40]

$$N_i(t) = \sum_j \int I_{ij} dt \tag{5}$$

Here the subscript i refers to the ith layer and j runs over the other components of the system. Thus, taking into account the definition of the current between two parts (i-j) of the system defined by the Transfer Hamiltonian approach in Eq. 1, it is possible to get a set of integro-differential equations for the charge evolution in time as shown in Eq. 6.

$$\begin{aligned}\frac{dN_i}{dt} = \frac{4\pi q}{\hbar}\Big(\int T_{Li}\rho_L\rho_i(f_L - n_i)dE + \int T_{Ri}\rho_R\rho_i(f_R - n_i)dE \\ + \sum_{j\neq i}^{(N-1)} \int T_{ji}\rho_j\rho_i(n_j - n_i)dE\Big) \quad , \quad \forall_i = 1\ldots N\end{aligned} \tag{6}$$

The above equation shows all the current term contributions i.e. contributions from the electrodes (first and second term) and the contribution of all neighbor layers (j) with the layer under study (i) (last term).[40,45]

Using semiclassical and one-dimension Wentzel-Kramers-Brillouin (WKB) approximation for transmission coefficients and taking into account electron and hole carrier contributions with no inelastic scattering,[40,45] it was possible to set a rate equation system to solve the unknown distribution functions for each layer (transport and QDs) by evolving Eq. 6 to the steady state.

4.2.2 DOS (Density of States).

Quantum dots. Following again Illera *et al.* work‘s, a simplified model to represent the discrete energy levels ϵ_i in the QDs, based on finite spherical potential well approach was used (applied for the conduction band (CB) and valence band (VB)).[42] The number of binding states and their energetically position depend on the height of the well V_0, the radius R of the QD and the electron effective masses (in the core [$m_{core}^{e/h}$] and in the shell [$m_{shell}^{e/h}$]).

$$\cot(x) = -\sqrt{\frac{m_{shell}^{*}}{m_{core}^{*}}}\sqrt{\left(\frac{\sigma_0}{x}\right)^2 - 1} \quad \text{,where}$$

$$\sigma_0 = \sqrt{\frac{2m_{core}^{*}V_0}{\hbar^2}R^2} \quad \text{and} \quad x = \sqrt{\frac{2m_{core}^{*}}{\hbar^2}R^2\epsilon_i} \quad (7)$$

Eq. 7 does not have an analytical solution and numerical methods need to be used to solve it.[45,49] The solutions of Eq. 7 contain the discrete binding energy levels ϵ_i of the QD.

It is worth saying that the energy level solutions above need to be shifted. Particularly, since the Schrödinger equation gives the zero energy origin located at the bottom of the well, it becomes essential to shift the energy ϵ_i proportional to the bulk band gap E_g so as to have a common Fermi level. Therefore, it is possible to define

$$\epsilon_i' = \epsilon_i + E_{shift} \quad (8)$$

where E_{shift} is proportional to bulk band gap E_g.

Once the discrete energy levels of the QDs have been calculated and following the definition of the DOS for these kinds of nanostructures, it is possible to define the DOS as,

$$\rho(E) = \sum_i^n \frac{\frac{\gamma}{2\pi}}{(E - \epsilon_i')^2 + \left(\frac{\gamma}{2\pi}\right)^2} \quad (9)$$

where γ is the broadening of the level and it is related to the tunnel probabilities.[42,45]

Transport layers. It is necessary to make the same study for the transport layer to conform the whole QLED system. Transport layers could be considered as different structures than QDs. Then, infinite potential wells under EMA (Effective Mass Approximation) approach were considered to calculate the energy level spectra. This first approach is the simplest example of quantum well.[49] Thus, for a quantum well of width a, the energy levels associated are the following ones

$$\epsilon_i = \frac{\hbar^2 \pi^2 i^2}{2 m^* a^2} \tag{10}$$

where the integer i ∈ N is the quantum number that labels the states.[49]

Finally, and following the definition of DOS for these kinds of 2D dimensional nanostructures,[50] it is possible to define the DOS as

$$\rho\left(E\right)^{2D} = \frac{m^*}{\pi \hbar^2} \sum_{i=1}^{n} \Theta\left(E - \epsilon_i\right) \tag{11}$$

where ϵ_i are the energies quantized states and $\Theta(E - \epsilon_i)$ is the step function.[50]

4.2.3 Potential energy.

As can be extracted from Fig. 8, each QLED junction was modeled as a current tunnel junction in parallel with a capacity. These capacities represent the electrostatic influence between the different parts of the system.[42]

Following Illera *et al.* work and generalizing the same strategy relating to electron-electron interaction, not only for QDs but for the transport layers of the QLED device, it is possible to evaluate the change in the local potential V_i for all layers (QDs and transport).Therefore, electron-electron interaction due to injected charge is included directly by the solution of the Poisson equation Eq. 12.

$$\overrightarrow{\nabla} \cdot \left(\varepsilon_r \overrightarrow{\nabla} V_i\right) = -\frac{q \Delta N_i}{\Omega} \tag{12}$$

where ϵ_r is the relative permittivity of the dielectric media and Ω is the layer volume. ΔN_i is the change in the number of electrons, calculated respect to the number of electrons N_0 initially in the ith layer.[51]

Likewise, the general solution of the Poisson equation for the local potential energy i.e.

U_i=-qV_i of each layer can be written as follows.[51]

$$U_i = \sum_{j \neq i} \frac{C_{ij}}{C_{tot,i}} (-qV_j) + U_{0i}\ \Delta N_i \quad \text{,where}$$

$$C_{tot,i} = \sum_{j, j \neq i} C_{ij} \quad \text{and} \quad U_{0i} = \frac{q^2}{C_{tot,i}} \qquad (13)$$

where the subscript j runs over all the components of the system, C_{ij} is the capacitive coupling between the ith and jth component and $C_{tot,i}$ is the total capacitive coupling of ith layer. Moreover, the charge energy constant U_{0i} is the potential increase as a consequence of the injection of one electron into the layer (QD or transport layer).

4.2.4 Self consistent solution.

Once this point was reached, all elements that take part in the whole transport mechanism through the Transfer Hamiltonian approach were analyzed. Yet, as it can be deduced from the equations Eq.(4),(9),(11) and (13), there are dependencies among them. It means that it is necessary to enter in a self consistent field in order to get a final solution value.

The flowchart and algorithm implemented is depicted in Fig. 9.

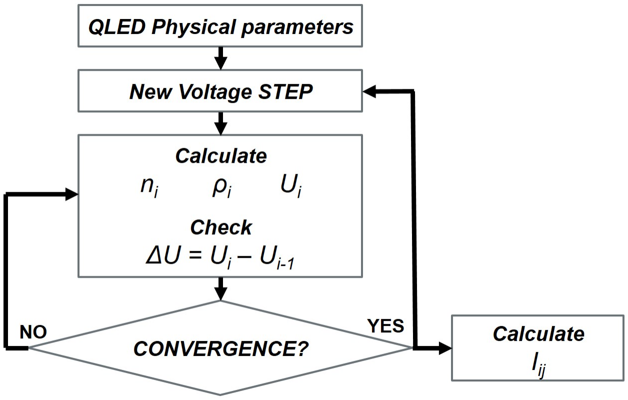

Figure 9: . Self consistent field algorithm implemented.

4.3 Simulations Results

Once the theoretical background behind the QLED modelling was established and the algorithm proposed to implement the latter was codified in the software, the current density, the total QLED current, the electronic charge density evolution and the band diagram of the device were extracted from the *QLEDsim* simulator. Thereby, Fig. 10 shows the physical modelling carried out for the QLED device where all geometrical parameters were extracted from the experimental part.

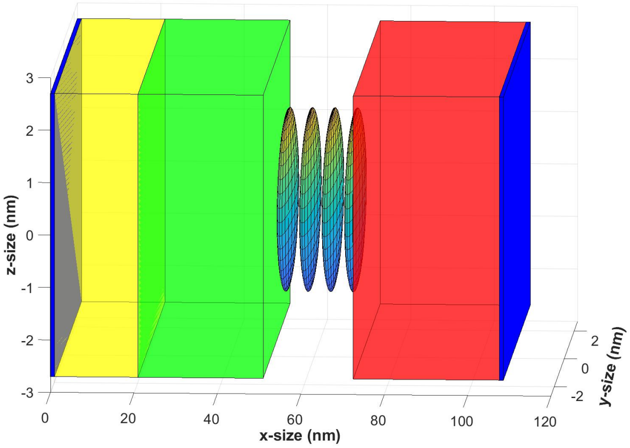

Figure 10: 3D view for QLED model with all transport layer form experimental device introduced i.e. Anode/HIL/HTL/QDs/ETL/Cathode. NB: the quantum dots represented in the figure are spherical. Different scales were used in each direction for the sake of clarity.

Table 3 presents all experimental parameter values used in the simulation.[35,52–68]

Table 3: QLED Layers (ANODE-HIL-HTL-EL-ETL-CATHODE) bulk material properties.

LAYER	$\epsilon_r(\epsilon_0)$	$m_e^*(m_0)$	$m_h^*(m_0)$	E_A(eV)	E_i(eV)	ϕ(eV)	BG(eV)
ITO	-	-	-	-	-	4.70	-
PEDOT:PSS	17	0.25	1.30	3.60	5.30	4.50	1.70
TFB	15	0.25	1.30	2.60	5.50	4.50	2.90
$CuInS_2$(core)	8.7	0.16	1.30	4.36	5.86	5.36	1.50
ZnS(shell)	8.9	0.28	0.61	3.90	7.80	6.30	3.90
ZnO	8.5	0.23	1.21	4.30	7.67	5.30	3.37
Al	-	-	-	-	-	4.30	-

4.3.1 Theoretical vs Experimental.

The current density curve versus the bias voltage applied to the device was simulated taking into account the QLED device area of QD diameter(core/shell from Table 1). Moreover, after obtaining the current density for the QLED modelling, it was possible to make the approximation to the real 3D device. This approximation was based on ballistic behavior on the system and the way followed, as a first approach, was to multiply the current density by the area given in individual pixels from QLED manufactured experimentally. This pixel area is set to 4.5mm^2.

Both experimental and theoretical I-V results were compared and presented in Fig. 11. In conclusion, it can be seen that simulated I-V curve keeps in the experimental range of curves measured from the 6-pixel QLED device manufactured.

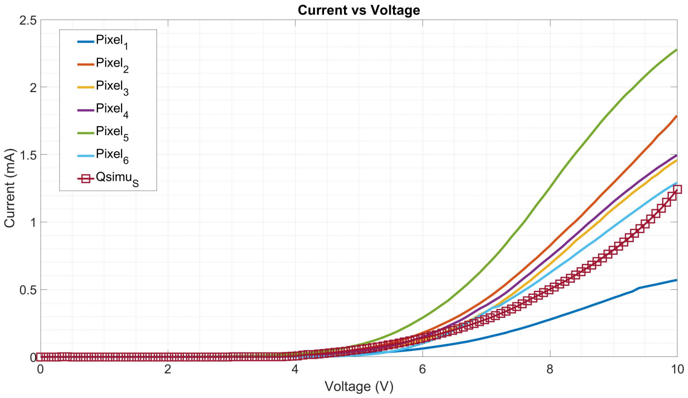

Figure 11: . Experimental curve for the 6-pixel QLED device manufactured compared to the simulated curve (red-square line) obtained from *QLEDsim* simulator.

4.3.2 Band Diagram.

Fig. 6 showed the proposed energy levels from vacuum level. Thus, using the bulk material values from Table 3 of electron affinity and band gaps shown, it is possible to follow "electron affinity rule" and band alignment[69] at the different material junctions to depict the heterojunction band diagram in both equilibrium and dynamic state.

Equilibrium band diagram of the heterojunction. The band diagram of the heterojunction in equilibrium for the conduction band (CB) and valence band (VB) i.e. when those materials are put in contact (with no bias voltage applied) is presented in Fig. 12. Here, the Fermi level in equilibrium is placed at the y-axis origin (Ef_0=0eV). The goal is to give an illustration of the band diagram shape of the heterojunction in a relative way and not in an absolute definition.

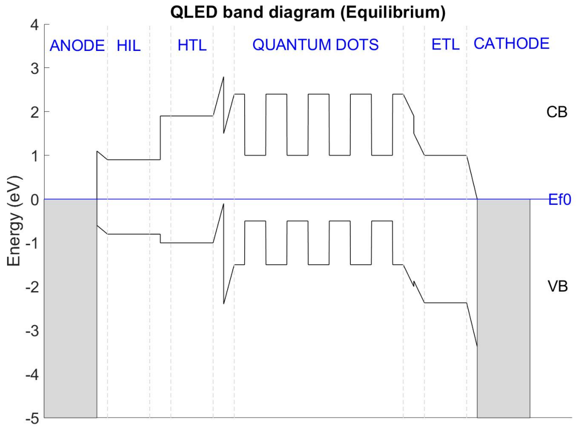

Figure 12: . Equilibrium band diagram of the heterojunction from *QLEDsim*.

Dynamic band diagram of the heterojunction. Now QLED forward biased was considered i.e. a voltage V>0 was applied to the electrodes. Therefore, the system was out of the equilibrium and as any heterojunction system, the band diagram was modified with the voltage applied. Thanks to *QLEDsim* simulator, it is possible to calculate the potential energy increase in each layer allowing us to draw the following Fig. 13 for each bias voltage step for V=[2,5,8,10]V. Fig. 12 (equilibrium) and Fig. 13 (biased) depict the conduction and valence band profiles when the potential (calculated from Eq. 13) is considered. The equation yields the potential in each device layer, the details of the potential profile within each layer are not represented. Each core/shell quantum dot layer is considered as a single-material layer, and therefore the potential profile representation within the quantum dots should not be considered as an accurate representation.

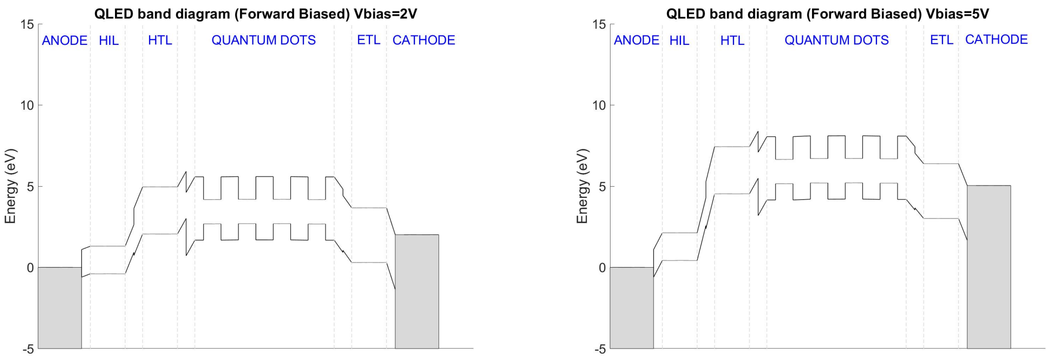

(a) QLED forward biased (V=2V)

(b) QLED forward biased (V=5V)

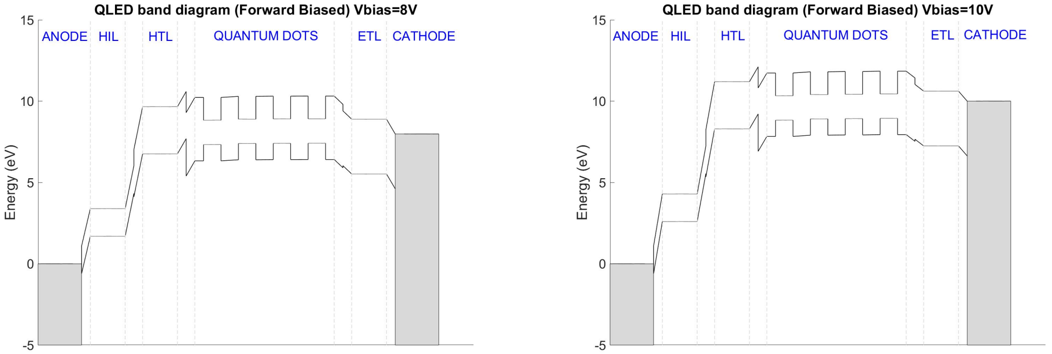

(c) QLED forward biased (V=8V)

(d) QLED forward biased (V=10V)

Figure 13: . Dynamic band diagram of the heterojunction.

4.3.3 Accumulated charge distribution.

Once the QLED is out of equilibrium and the band diagram was described, the accumulated charge distribution in each layer was depicted for each voltage step taken. Thereby, it is possible to calculate the variation of number of electrons (ΔN=N-N$_0$) for each voltage step. That relationship indicates the variation of electrons (N) respect to the initial number (N$_0$). That initial value of the charge is obtained at zero bias voltage in equilibrium state. Thus, if the variation is negative, it implies that the system loses charge (hole accumulation). On the other hand, if the variation is positive, the system increases its charge (electron accumulation).[42,45] Therefore, the following Fig. 14 describes the accumulated charge for each layer depending on the voltage step variation applied dynamically. Furthermore, that accumulated charge for each layer out of the equilibrium is represented from a graphical colormap description in Fig. 15.

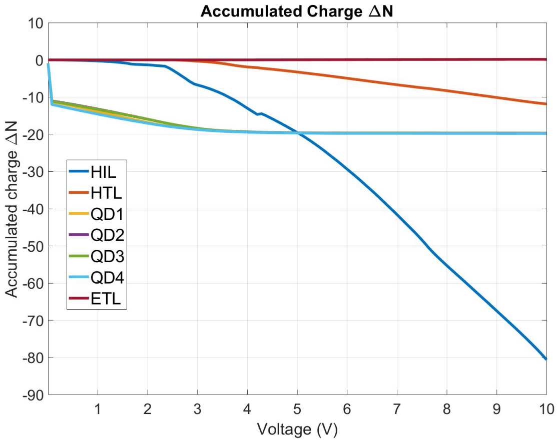

Figure 14: . QLED accumulated charge for each layer.

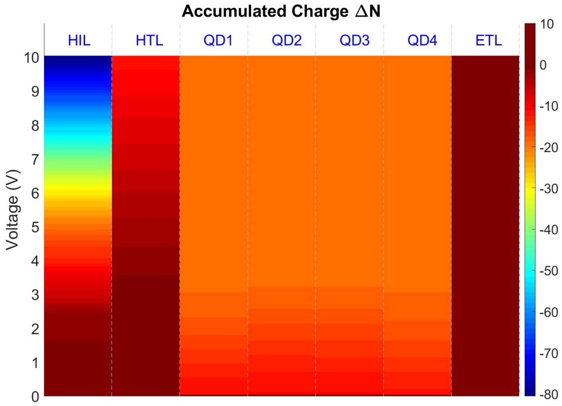

Figure 15: . QLED graphical color mapping of accumulated charge.

4.4 Validity of Simulation Model

Although the numerical data are validated experimentally and are in good agreement with the experiment results, we would like to highlight some of the limitations of the present simulator developed.

4.4.1 Radiative recombination.

The actual theoretical model does not deal with this topic in the present simulator version. In order to introduce the latter, a generation/recombination rate might be incorporated in

Eq.(6). Yet, we decided to postpone this study due to the relative low visible radiative phenomena of the device and the good agreement obtained with the experimental results.

4.4.2 Density of States.

DOS is key to calculate the final I-V curve of the system. In the current computational model, some basic approaches have been used depending on the subsystems treated i.e. quantum dots and transport layers.

Thereby, DOS for QDs elements are calculated based on the use of a Lorentzian shape to introduce the broadening of the discrete energy levels as shown in Eq.(9). On the other hand, transport layers could be considered as different structures from QDs and they have been identified as two-dimensional materials. For these kinds of 2D dimensional confinement nanostructures, DOS was defined in Eq.(11).

However, other techniques as *ab-initio* methods like DFT (Density Functional Theory) could give more accurate results when comparing with reality. Thus, a more realistic modelling for DOS might help to improve the QLED simulator results.

4.4.3 Thermal Dissipation.

From a macroscopic point of view, heat dissipation might play an important role when designing the QLED device for real applications, particularly for automotive lighting ones. Yet, thermal dissipation features were not considered in the current computational model, since the characterization of the experimental QLED fabricated was performed in a short period of time i.e. electrical characterization was made through SMU laboratory tool in a matter of seconds. Therefore, the influence of self heating in the I-V figure was considered negligible for the objective of this work, and the good agreement between experimental and simulation results seems to support our approach.

4.4.4 Electrode Interface Capacitance.

As shown in Eq. 13, the solution of the Poisson equation in our model for the local potential can be divided in two terms. The first one is called the Laplace term[42,51] and it contains the capacitive couplings between the different layers of the QLED device. These capacitive couplings have an important contribution in the final QLED current since they dominate the DOS shift, changing therefore the number of energy levels which might contribute to the transport process.[42]

Furthermore, our model shows that the junction capacitance at the interface between the electrodes and the related transport layers plays an important role in the I-V performance, specifically in both the current device capability and the QLED turn-on voltage parameters. Particularly, Anode-HIL interface capacitance has a greater influence in the I-V plot shape.

Thereby, the Fig. 16 proves how these two parameters i.e. current capability and turn-on voltage can be modified by adjusting the interface capacitance at the anode side. Thanks to the QLED simulator developed, this task can be carried out easily by either changing the transport layers or directly estimating that impact of the capacitance value in the whole model system.

It is worth saying that the values of capacitance used in our work for Anode-HIL interface are the same order of magnitude than the capacitances given by the Coulomb blockade effect in similar systems. Moreover, those values are below the maximum capacitance per unit area (C_{max}) reported by Islam *et al.*[70,71] and shown in Eq.(14).

$$C_{max} = \frac{\epsilon_r \epsilon_0}{t} \tag{14}$$

where ϵ_r is the relative permittivity of the dielectric media, ϵ_0 is the free space permittivity and t is the layer thickness.

Eventually, in order to help to design a real QLED device, that Anode-HIL interface capacitance should be put under control. Firstly during the manufacturing process (HIL layer deposition on the anode electrode by using accurate thin-film deposition techniques) to have uniform layers which would lead to the same I-V characteristics for all pixels built on the same substrate. And secondly, by modifying that capacitance value through some kind of the transport layers doping, which could give an optimal charge injection balance into the

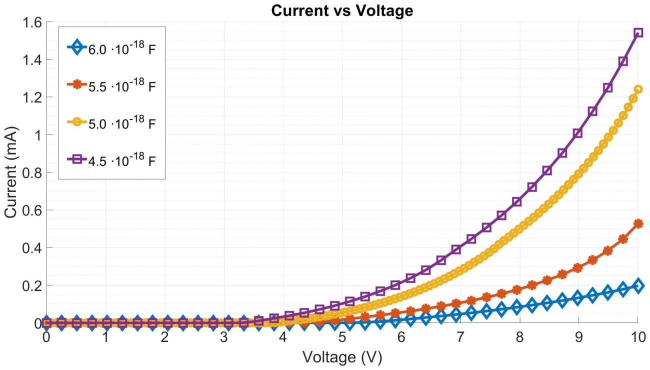

Figure 16: . I-V QLED plot varying Anode-HIL interface capacitance.

device.

4.4.5 Quantum Dot size.

Another topic to bear in mind is the variation of current transport with the QD size. As reported in the literature, a current increase with the dot size is expected since both the DOS of QDs and the conduction gap have a strong influence in the final current. Specifically, as size increases, the available states inside the nanoparticles increases, while the QD band gap decreases due to relaxation of quantum confinement. Those effects contribute to increasing the current with the dot size.[44]

5 Conclusions

An electroluminescence device, i.e. a 6-pixel (4.5mm^2/pixel) QLED system, based on characterized $CuInS_2/ZnS$ QDs was designed and fabricated with a conventional structure: ITO as anode, PEDOT:PSS (HIL), TFB (HTL), $CuInS_2/ZnS$ QDs(EL), ZnO NPs (ETL) and Al layer as cathode. In addition, each pixel was electrically characterized to obtain the electrical I-V curve, which gives some insight about how the fabrication process and layer thickness have an influence in the shape of the plot.

Furthermore, a computational model based on the Transfer Hamiltonian approach to describe the electrical behavior of the lighting system was presented. Thus, I-V curve was simulated and compared with experimental results, reaching a remarkable agreement as shown in Fig. 11.

The influence of critical parameters as the junction capacitance between the anode and the HIL layer was studied in the simulator to report the close relation of I-V curve with the fabrication process relating to the thickness and material type which conform the electroluminescent device.

That variability in the fabrication process step has a huge influence in the device performance, specifically in the current flowing throughout the device. Therefore, the computational model offers the possibility to model an electroluminescent QLED device by anticipating the electrical performance in a theoretical design step before going to the automotive QLED manufacturing at the laboratory.

To conclude, QLEDs might offer a great advantage in the automotive field, offering the possibility of using this technology worldwide in automotive applications such as interior and exterior lighting products. Thus, starting by the development of an experimental device along with a good electrical simulation behavior, the QLED model developed could set the basis for further research on the field of vehicle lighting systems.

6 Acknowledgements

This work was supported by VALEO, multinational automotive company. F.M.G.C and S.R.B were supported by Project ENE2016_80944_R, funded by the Spanish Ministerio de Economía, Industria y Competitividad. The authors thankfully acknowledge the computational assistance provided by Sergio Illera.

References

(1) LEDs Magazine, Technology and applications of light emitting diodes, LEDs Magazine, Volume 10, Issue 7. *Technology and applications of light emitting diodes* **2013**, *10*, 1.

(2) Boulay, P. Automotive Lighting Technology, Industry and Market Trends 2017 Report. *Automotive Lighting Technology, Industry and Market Trends 2017 Report* **2017**,

(3) Wood, V.; Bulović, V. Colloidal quantum dot light-emitting devices. *Nano Reviews* **2010**, *1*, 5202.

(4) Tessier, M. D.; Dupont, D.; De Nolf, K.; De Roo, J.; Hens, Z. Economic and Size-tunable Synthesis of InP/ZnE (E = S,Se) Colloidal Quantum Dots. *Chemistry of Materials* **2015**, *3*, 150611083950009.

(5) Xu, G.; Zeng, S.; Zhang, B.; Swihart, M. T.; Yong, K. T.; Prasad, P. N. New Generation Cadmium-Free Quantum Dots for Biophotonics and Nanomedicine. *Chemical Reviews* **2016**, *116*, 12234–12327.

(6) Xu, S.; Ziegler, J.; Nann, T. Rapid synthesis of highly luminescent InP and InP/ZnS nanocrystals. *Journal of Materials Chemistry* **2008**, *18*, 2653.

(7) Ippen, C.; Greco, T.; Wedel, A. InP/ZnSe/ZnS: A Novel Multishell System for InP Quantum Dots for Improved Luminescence Efficiency and Its application in a Light-Emitting Device. *Journal of Information Display* **2012**, *13*, 91–95.

(8) Li, L.; Pandey, A.; Werder, D. J.; Khanal, B. P.; Pietryga, J. M.; Klimov, V. I. Efficient synthesis of highly luminescent copper indium sulfide-based core/shell nanocrystals with surprisingly long-lived emission. *Journal of the American Chemical Society* **2011**, *133*, 1176–1179.

(9) Deng, D.; Chen, Y.; Cao, J.; Tian, J.; Qian, Z.; Achilefu, S.; Gu, Y. High-Quality CuInS 2 /ZnS Quantum Dots for In vitro and In vivo Bioimaging. *Chemistry of Materials* **2012**, *24*, 3029–3037.

(10) Liu, S.; Zhang, H.; Qiao, Y.; Su, X. One-pot synthesis of ternary CuInS2 quantum dots with near-infrared fluorescence in aqueous solution. *RSC Advances* **2012**, *2*, 819.

(11) Li, L.; Daou, T. J.; Texier, I.; Kim Chi, T. T.; Liem, N. Q.; Reiss, P. Highly Luminescent CuInS 2 /ZnS Core/Shell Nanocrystals: Cadmium-Free Quantum Dots for In Vivo Imaging. *Chemistry of Materials* **2009**, *21*, 2422–2429.

(12) Li, S.; Chen, Y.; Huang, L.; Pan, D. Simple continuous-flow synthesis of Cu–In–Zn–S/ZnS and Ag–In–Zn–S/ZnS core/shell quantum dots. *Nanotechnology* **2013**, *24*, 395705.

(13) Chen, Y.; Li, S.; Huang, L.; Pan, D. Green and Facile Synthesis of Water-Soluble Cu-In-S/ZnS Core/Shell Quantum Dots. *Inorganic Chemistry* **2013**, *52*, 12–14.

(14) Xiong, W. W.; Yang, G. H.; Wu, X. C.; Zhu, J. J. Aqueous synthesis of color-tunable CuInS2/ZnS nanocrystals for the detection of human interleukin 6. *ACS Applied Materials and Interfaces* **2013**, *5*, 8210–8216.

(15) Kim, J. H.; Yang, H. High-Efficiency Cu-In-S Quantum-Dot-Light-Emitting Device Exceeding 7%. *Chemistry of Materials* **2016**, *28*, 6329–6335.

(16) Ogawa, T.; Kuzuya, T.; Hamanaka, Y.; Sumiyama, K. Synthesis of Ag-In binary sul-

fide nanoparticles-structural tuning and their photoluminescence properties. *Journal of Materials Chemistry* **2010**, *20*, 2226–2231.

(17) Hamanaka, Y.; Ozawa, K.; Kuzuya, T. Enhancement of Donor - Acceptor Pair Emissions in Colloidal AgInS 2 Quantum Dots with High Concentrations of Defects. *Journal of Physical Chemistry C* **2014**, *118*, 1456214568.

(18) Mao, B.; Chuang, C.-h.; McCleese, C.; Zhu, J.; Burda, C. Near-Infrared Emitting AgInS 2 /ZnS Nanocrystals. *The Journal of Physical Chemistry C* **2014**, 140611152129000.

(19) Torimoto, T.; Adachi, T.; Okazaki, K.-I.; Sakuraoka, M.; Shibayama, T.; Ohtani, B.; Kudo, A.; Kuwabata, S. Facile synthesis of ZnS-AgInS2 solid solution nanoparticles for a color-adjustable luminophore. *Journal of the American Chemical Society* **2007**, *129*, 12388–12389.

(20) Subramaniam, P.; Lee, S. J.; Shah, S.; Patel, S.; Starovoytov, V.; Lee, K. B. Generation of a library of non-toxic quantum dots for cellular imaging and siRNA delivery. *Advanced Materials* **2012**, *24*, 4014–4019.

(21) Deng, D.; Qu, L.; Zhang, J.; Ma, Y.; Gu, Y. Quaternary Zn-Ag-In-Se Quantum Dots for Biomedical Optical Imaging of RGD-Modi fi ed Micelles. *ACS Appl. Mater. Interfaces* **2013**, 8.

(22) Srivastava, B. B.; Jana, S.; Karan, N. S.; Paria, S.; Jana, N. R.; Sarma, D. D.; Pradhan, N. Highly luminescent Mn-doped ZnS nanocrystals: Gram-scale synthesis. *Journal of Physical Chemistry Letters* **2010**, *1*, 1454–1458.

(23) Abib, M.; Yao, X.; Li, G.; Mi, L.; Chang, Y.; Wang, H.; Yu, D.; Jiang, Y. Simulation-Based Optical Spectra Analyses and Synthesis of Highly Monodispersed Mn-Doped ZnSe Nanocrystal. *Nano* **2016**, *11*, 13–15.

(24) Wu, X.; Tian, F.; Wang, W.; Chen, J.; Wu, M.; Zhao, J. X. Fabrication of highly fluorescent graphene quantum dots using L-glutamic acid for in vitro/in vivo imaging and sensing. *Journal of materials chemistry. C, Materials for optical and electronic devices* **2013**, *1*, 4676–4684.

(25) Sugimoto, H.; Fujii, M.; Fukuda, Y.; Imakita, K.; Akamatsu, K. All-inorganic water-dispersible silicon quantum dots: highly efficient near-infrared luminescence in a wide pH range. *Nanoscale* **2014**, *6*, 122–6.

(26) Ozdemir, S.; Suyolcu, Y. E.; Turan, S.; Aslan, B. Influence of the growth conditions on the optical and structural properties of self-assembled InAs/GaAs quantum dots for low As/In ratio. *Applied Surface Science* **2017**, *392*, 817–825.

(27) Vo, Q. H.; Watanabe, K.; Kageyama, T.; Iwamoto, S.; Arakawa, Y. Self-assembled formation of GaAsP nano-apertures above InAs/GaAs quantum dots by the thermal diffusion of phosphorus. *Physica Status Solidi (B) Basic Research* **2016**, *253*, 659–663.

(28) Grigel, V.; Dupont, D.; De Nolf, K.; Hens, Z.; Tessier, M. D. InAs Colloidal Quantum Dots Synthesis via Aminopnictogen Precursor Chemistry. *Journal of the American Chemical Society* **2016**, *138*, 13485–13488.

(29) Franke, D.; Harris, D. K.; Chen, O.; Bruns, Continuous injection synthesis of indium arsenide quantum dots emissive in the short-wavelength infrared. *Nature Communications* **2016**, *7*, 12749.

(30) Khafajeh, R.; Molaei, M.; Karimipour, M. Synthesis of ZnSe and ZnSe: Cu quantum dots by a room temperature photochemical (UV-assisted) approach using Na2SeO3 as Se source and investigating optical properties. *Luminescence* **2016**, 1–7.

(31) Herrera, M.; Chisholm, M. F.; Kamarudin, M. A.; Zhuang, Q. D.; Hayne, M.; Molina, S. I. Effect of an in-situ thermal annealing on the structural properties of

self-assembled GaSb / GaAs quantum dots. *Applied Surface Science* **2016**, *395*, 136–139.

(32) Kruppa, M.; Thomas, W.; Huhn, W. An OLED taillight revolution: From point light sources to segmented area light sources. *Information Display* **2019**, *35*, 14–18.

(33) Margulies, E. A.; Boudreauit, P. L. T.; Adamovich, V. I.; Alleyne, B. D.; Weaver, M. S.; Brown, J. J. Narrow spectrum deep red emitters for OLED lighting and display. *Digest of Technical Papers - SID International Symposium* **2019**, *50*, 911–913.

(34) Kim, H. Y.; Park, Y. J.; Kim, J.; Han, C. J.; Lee, J.; Kim, Y.; Greco, T.; Ippen, C.; Wedel, A.; Ju, B. K.; Oh, M. S. Transparent InP Quantum Dot Light-Emitting Diodes with ZrO2 Electron Transport Layer and Indium Zinc Oxide Top Electrode. *Advanced Functional Materials* **2016**, *26*, 3454–3461.

(35) Kim, J.-H.; Yang, H. All-solution-processed, multilayered CuInS_2/ZnS colloidal quantum-dot-based electroluminescent device. *Optics Letters* **2014**, *39*, 5002.

(36) Bai, Z.; Ji, W.; Han, D.; Chen, L.; Chen, B.; Shen, H.; Zou, B.; Zhong, H. Hydroxyl-Terminated CuInS2 Based Quantum Dots: Toward Efficient and Bright Light Emitting Diodes. *Chemistry of Materials* **2016**, *28*, 1085–1091.

(37) Liu, Z.; Zhao, K.; Tang, A.; Xie, Y.; Qian, L.; Cao, W.; Yang, Y.; Chen, Y.; Teng, F. Solution-processed high-efficiency cadmium-free Cu-Zn-In-S-based quantum-dot light-emitting diodes with low turn-on voltage. *Organic Electronics* **2016**, *36*, 97–102.

(38) Ossila, OPV and OLED Fabrication Guide. 2017; https://www.ossila.com/pages/organic-photovoltaic-opv-and-organic-light-emitting-diode-oled-fabrication-manual.

(39) Islam, S. M.; Biswas, P.; Banerji, P.; Chakraborty, S. InAs quantum dots as charge

storing elements for applications in flash memory devices. *Materials Science and Engineering B: Solid-State Materials for Advanced Technology* **2015**, *198*, 102–107.

(40) Illera, S.; Garcia-Castello, N.; Prades, J. D.; Cirera, A. A transfer Hamiltonian approach for an arbitrary quantum dot array in the self-consistent field regime. *Journal of Applied Physics* **2012**, *112*, 1–8.

(41) Illera, S.; Prades, J. D.; Cirera, A.; Cornet, A. Transport in quantum dot stacks using the transfer Hamiltonian method in self-consistent field regime. *Epl* **2012**, *98*, 1–7.

(42) Illera, S.; Prades, J. D.; Cirera, A.; Cornet, A. A transfer Hamiltonian model for devices based on quantum dot arrays. *Scientific World Journal* **2015**, *2015*, 1–20.

(43) Illera, S.; Prades, J. D.; Cirera, A. A compact theoretical model for opto-electronic devices based on quantum dot arrays. *arXiv:1305.3612 [cond-mat.mes-hall]* **2013**, 1–14.

(44) Garcia-Castello, N.; Illera, S.; Guerra, R.; Prades, J. D.; Ossicini, S.; Cirera, A. Silicon quantum dots embedded in a SiO2 matrix: From structural study to carrier transport properties. *Physical Review B - Condensed Matter and Materials Physics* **2013**, *88*, 1–11.

(45) Robles, S. I. Electron transport in low-dimensional systems : optoelectronic device simulations. Ph.D. thesis, Universitat de Barcelona, 2015.

(46) Prange, R. E. Tunneling from a many-particle point of view. *Physical Review* **1963**, *131*, 1083–1086.

(47) Passoni, M.; Bottani, C. E. Transfer Hamiltonian analytical theory of scanning tunneling spectroscopy. *Physical Review B - Condensed Matter and Materials Physics* **2007**, *76*, 1–14.

(48) Noguera, C. Validity of the transfer Hamiltonian approach : application to the STM spectroscopic mode. *Journal de Physique* **1989**, *50*, 2587–2599.

(49) Davies, J. H. *The Physics of Low- Dimensional Semiconductors: An Introduction.*; Cambridge University Press, 1998.

(50) Deliyannis, P. C. Density of states. *Journal of Mathematical Physics* **1971**, *12*, 860–862.

(51) Datta, S. Electrical resistance: An atomistic view. *Nanotechnology* **2004**, *15*.

(52) Huang, P. R.; He, Y.; Cao, C.; Lu, Z. H. The origin of the high work function of chlorinated indium tin oxide. *NPG Asia Materials* **2013**, *5*, 1–5.

(53) Bednarski, H.; Hajduk, B.; Jurusik, J.; Jarzabek, B.; Domanski, M.; Łaba, K.; Wanic, A.; Łapkowski, M. The influence of PEDOT to PSS ratio on the optical properties of PEDOT: PSS thin solid films - Insight from spectroscopic ellipsometry. *Acta Physica Polonica A* **2016**, *130*, 1242–1244.

(54) Muckley, E. S.; Jacobs, C. B.; Vidal, K.; Mahalik, J. P.; Kumar, R.; Sumpter, B. G.; Ivanov, I. N. New Insights on Electro-Optical Response of Poly(3,4-ethylenedioxythiophene):Poly(styrenesulfonate) Film to Humidity. *ACS Applied Materials and Interfaces* **2017**, *9*, 15880–15886.

(55) Zheng, Q.; Sun, J.; Cheng, S.; Lai, Y.; Zhou, H.; Yu, J. Power conversion efficiency enhancement of polymer solar cells using MoO3/TFB as hole transport layer. *Applied Physics A: Materials Science and Processing* **2015**, *120*, 857–861.

(56) Ahn, D. A.; Lee, S.; Chung, J.; Park, Y.; Suh, M. C. Impact of Interface Mixing on the Performance of Solution Processed Organic Light Emitting Diodes - Impedance and Ultraviolet Photoelectron Spectroscopy Study. *ACS Applied Materials and Interfaces* **2017**, *9*, 22748–22756.

(57) Shabaev, A.; Mehl, M. J.; Efros, A. L. Energy band structure of CuInS2 and optical spectra of CuInS2 nanocrystals. *Physical Review B - Condensed Matter and Materials Physics* **2015**, *92*, 1–9.

(58) Look, D. C.; Manthuruthil, J. C. Electron and hole conductivity in CuInS2. *Journal of Physics and Chemistry of Solids* **1976**, *37*, 173–180.

(59) Krustok, J.; Raudoja, J.; Collan, H. Photoluminescence and the tetragonal distortion in CuInS2. *Thin Solid Films* **2001**, *387*, 195–197.

(60) Oda, M.; Miyaoka, T.; Yamada, S.; Tani, T. Synthesis, Characterization and its Photoluminescence Properties of Group I-III-VI2 CuInS2 nanocrystals. *Physics Procedia* **2012**, *29*, 18–24.

(61) Larsen, J. K.; Keller, J.; Lundberg, O.; Jarmar, T.; Riekehr, L.; Scragg, J. J.; Platzer-Bjorkman, C. Sulfurization of Co-Evaporated Cu(In,Ga)Se2 as a Postdeposition Treatment. *IEEE Journal of Photovoltaics* **2018**, *8*, 604–610.

(62) Ramli, H.; Abdul Rahim, S. K.; Abd Rahim, T.; Muhaimin Aminuddin, M. Optimization of zinc sulfide (ZnS) electron affinity in copper indium sulfide (Cis) based photovoltaic cell. *Chalcogenide Letters* **2013**, *10*, 189–195.

(63) Uzar, N.; Arikan, M. C. Synthesis and investigation of optical properties of ZnS nanostructures. *Bulletin of Materials Science* **2011**, *34*, 287–292.

(64) Technology, P. Synthesis of stable and non-cadmium containing quantum dots conjugated with folic acid for imaging of cancer cells. *Poznan University of Medical Science* **2011**, 1–216.

(65) Properties, M. zinc oxide (ZnO) zinc oxide (ZnO). *AZO Materials* **2013**, 1–5.

(66) Tharsika, T.; Haseeb, A. S.; Akbar, S. A.; Mohd Sabri, M. F.; Hoong, W. Y. Enhanced ethanol gas sensing properties of SnO2-core/ZnO-shell nanostructures. *Sensors (Switzerland)* **2014**, *14*, 14586–14600.

(67) Oshikiri, M.; Imanaka, Y.; Aryasetiawan, F.; Kido, G. Comparison of the electron effective mass of the n-type ZnO in the wurtzite structure measured by cyclotron resonance and calculated from first principle theory. *Physica B: Condensed Matter* **2001**, *298*, 472–476.

(68) Vamsa, B.; Min, M. Y. O.; Dean, SIMULATION STUDY AND PERFORMANCE ANALYSIS OF n-ZnO/p-Si HETEROJUNCTION PHOTODETECTOR. *SSRN Electronic Journal* **2014**, *5*, 1–19.

(69) Rana, F. Chapter 2: Semiconductor Heterostructures. *Semiconductor Optoelectronics* **2011**, 1–29.

(70) Islam, S. M.; Banerji, P. Size effect of InAs quantum dots grown by metal organic chemical vapor deposition technique in storing electrical charges for memory applications. *RSC Advances* **2015**, *5*, 6906–6911.

(71) Islam, S. M.; Sarkar, K.; Banerji, P.; Sarkar, K. J.; Pal, B. Leakage current characteristics in MOCVD grown InAs quantum dot embedded GaAs metal-oxide-semiconductor capacitor. *RSC Advances* **2015**, *5*, 83837–83842.